Cardiovascular Engineering and Technology, Vol. 2, No. 2, June 2011 *(© 2011)* pp. 124–136
DOI: 10.1007/s13239-011-0041-y

The Distribution of Fluid Shear Stresses in Capillary Sprouts

*Peter C. Stapor, *Weixiong Wang, Walter L. Murfee, and Damir B. Khismatullin

Department of Biomedical Engineering, Tulane University, Lindy Boggs Center, Suite 500, New Orleans, LA 70118-5698, USA

(Received 28 September 2010; accepted 10 February 2011; published online 23 February 2011)

Associate Editor Laura Suggs oversaw the review of this article.

Abstract—Fluid shear stress has been implicated as a regulator of sprouting angiogenesis. However, whether endothelial cells within capillary sprouts *in vivo* experience physiologically relevant shear stresses remains unclear. The objective of our study is to estimate the shear stress distribution along the length of a capillary sprout through computational modeling of blood flow in a blind-ended channel branching off a host vessel. In this model, we use sprout geometries typical for the rat mesenteric microvasculature and consider three types of boundary conditions: (1) a non-permeable vessel wall, (2) a uniformly permeable vessel wall, and (3) a non-permeable vessel wall with open slots (representative of endothelial clefts). Our numerical simulation predicts that for each boundary condition a local maximum shear stress (13.9, 8.9, and 13.3 dyne cm^{-2}, respectively) occurs at the entrance of a 50 μm long, 6 μm diameter sprout branching at 90° off of a 11 μm diameter host vessel. The shear stress dropped below 0.2 dyne cm^{-2}, a threshold for endothelial cell activation, within 4.1 μm of the entrance for the non-permeable wall case and 4.2 μm for the uniformly permeable wall case. Shear stress magnitudes within the sprout were above 0.2 dyne cm^{-2} for longer sprout scenarios and peaked at 5.9 dyne cm^{-2} at endothelial cell clefts. These results provide a first estimate of relative fluid shear stress magnitudes along a capillary sprout and highlight the importance of investigating endothelial cell responses to flow conditions during angiogenesis in tumors and other altered microenvironments.

Keywords—Microcirculation, Angiogenesis, Endothelial cell, Shear stress, Capillary sprout, Computational fluid dynamics.

INTRODUCTION

Therapies aimed at manipulating microvascular growth require a full understanding of the cellular dynamics and environmental cues present during the formation of new capillaries from pre-existing vessels, termed angiogenesis. One potentially important signal in this process is fluid shear stress, which is present along the hierarchy of a microvascular network and has been implicated in vascular permeability, vessel enlargement, growth factor secretion, endothelial cell phenotypic regulation and the pathogenesis of atherosclerosis.[6,7,21,33] Increased shear stress has also been linked directly to angiogenesis by *in vivo* experiments demonstrating the increased number of capillaries in response to vasodilation.[23] While *in vitro* experiments have linked shear stress and shear stress gradients to endothelial cell proliferation,[22,36] migration,[10] cytoskeleton reorganization,[16] cell-matrix adhesion,[9] and soluble factor production,[4,24] their direct involvement in endothelial cell dynamics along a capillary sprout remains unclear.

Specific endothelial cell phenotypes and functions along capillary sprouts highlight the need to determine local environmental cues involved in angiogenesis. For example, tip cells have been identified vs. stalk cells.[18] Tip cells, which exist beyond the lumen of blind-ended vessels, play a role in sprout guidance and are phenotypically different than stalk cells, which are associated with the sprout's fluid filled lumen and contribute to cell proliferation and sprout elongation. The observation of fluid flow within blind-ended capillary sprouts[19] raises the question whether cells along the capillary sprout experience different shear stress magnitudes.

Given the experimental difficulty of observing velocity profiles at the micron and sub micron level *in vivo*, computational fluid dynamics (CFD) models have provided valuable information about local flow conditions in capillaries. Classical studies by Skalak *et al.* have evaluated the influence of rigid and elastic spheres on local flow in a straight tube.[34,37,38] Work by Secomb *et al.* has investigated the deformation of red blood cells during flow along cylindrical vessels[30] at bifurcations.[2] Most recently, Xiong and Zhang have

Address correspondence to Damir B. Khismatullin, Department of Biomedical Engineering, Tulane University, Lindy Boggs Center, Suite 500, New Orleans, LA 70118-5698, USA. Electronic mail: damir@tulane.edu

*P. C. Stapor and W. Wang contributed equally to this work.

determined the shear stress distribution along a non-permeable tube from the numerical simulation of deformable red blood cells flowing in narrow capillaries.[39] These studies support the use of similar theoretical approaches to determine shear stress magnitudes within a capillary sprout.

Since the issue of whether endothelial cells experience physiological shear stress stimuli during angiogenesis has not yet been addressed, the objective of our study was to estimate the distribution of shear stresses along the length of a capillary sprout. Using a three-dimensional (3D) finite volume method, we determined the velocity profile and shear stress distribution in blind-ended channels with physiologically relevant geometries branching from a host vessel. Based on simulations including wall permeability and the passing of a red blood cell by the sprout entrance, our analysis offers the first estimation of the wall shear stress (WSS) distribution during the initial stages of angiogenesis.

MATERIALS AND METHODS

Identification of Capillary Sprout Lumens

All experimental protocols were reviewed and approved by the Tulane University Animal Use and Care Committee. Adult male Wistar rats ($n = 2$; 340–360 g) were anesthetized with IM injection of ketamine (80 mg/kg bw) and xylazine (8 mg/kg bw). A bolus of 2 mL of fixable 40 kDa FITC-dextran (12.5 mg/mL, Invitrogen) was injected via the femoral vein in each rat ($n = 2$). Following the injection, the animals were sacrificed, and the mesenteric tissue was fixed *in situ* with 4% paraformaldahyde for 30 min. Mesenteric windows, defined as the thin translucent connective tissues between the mesenteric arterial/venous vessels feeding the bowel, were blindly harvested from the ileum section of the small intestine. The tissues were immediately placed in 10 mM phosphate buffered saline (PBS), and then mounted on positively charged glass slides. The rat mesentery was selected for this study because it allows for observation of capillary sprout geometries in an intact microvascular network. Tissues from each animal were labeled with an antibody against PECAM (CD31; BD Pharmingen) according to the following protocol: (1) one hour incubation at room temperature with 1:40 mouse monoclonal biotinylated CD31 (Serotec) antibody diluted in antibody buffer (0.1% Saponin in PBS + 2% BSA); (2) one hour incubation at room temperature with CY3-conjugated Streptavidin (Jackson ImmunoResearch Laboratories) antibody diluted in antibody buffer.

Images were captured with a 20× (Oil; NA = 0.8) or a 60× (Oil; NA = 1.4) inverted microscope (Olympus IX70) objective coupled with a PixelFly camera. The network montage (shown in Fig. 1a) was generated by overlaying sequential images using custom software. Capillary sprouts were defined as blind-ended vessels visualized by PECAM labeling. After sprouts were identified, individual 20× images of FITC-dextran were acquired. Sprout length, sprout diameter, host vessel diameter, and sprout angle from the host vessel were measured on images of FITC-dextran filled lumens using the Java-based NIH image

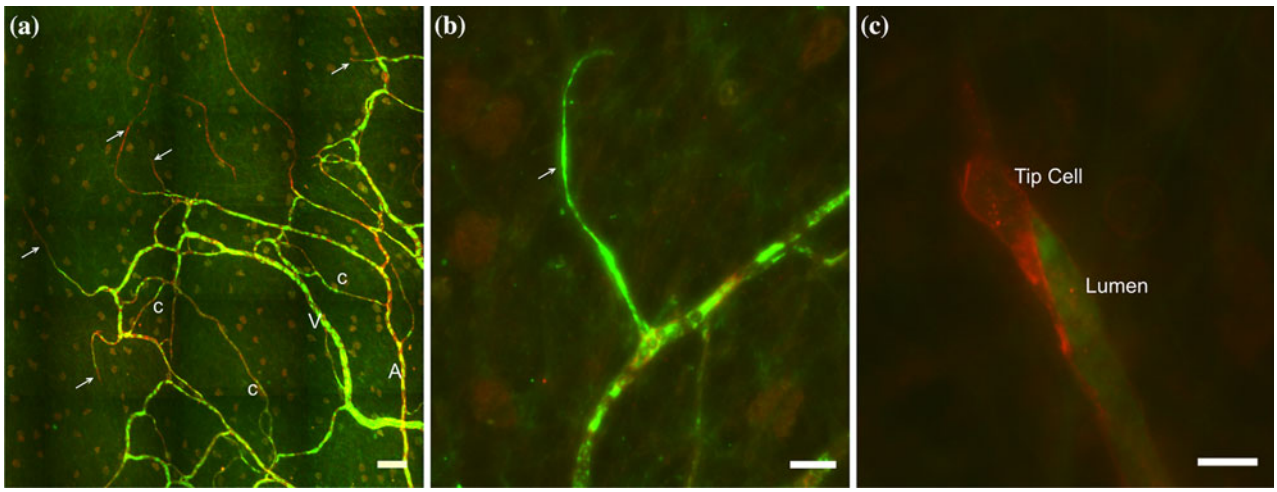

FIGURE 1. Identification of capillary sprout lumens with injected fixable 40 kDa FITC-dextran (green) in rat mesenteric microvascular networks immunolabeled for PECAM (red). (a) Representative montage of an unstimulated microvascular network region. Dextran injections identified the lumens of arterioles (A), venules (V), capillaries (c) and capillary sprouts (arrows). (b) FITC-dextran identifies sprout (arrow) lumen geometry branching from a host vessel. (c) A capillary sprout with PECAM expression extending past the dextran filled lumen (green). Scale bars = 100 μm (a), 25 μm (b) and 10 μm (c).

processing software ImageJ (version 1.43u, downloaded from http://rsbweb.nih.gov/ij/). 121 sprout lumens, from 9 tissues (at least 4 tissues per animal) were measured. Sprout length was measured down the centerline of fluorescent dextran. Sprout and host vessel diameters were measured at least twice to verify their lengths. Branching angles were measured from the centerline of the host vessel to centerline of the sprout lumen.

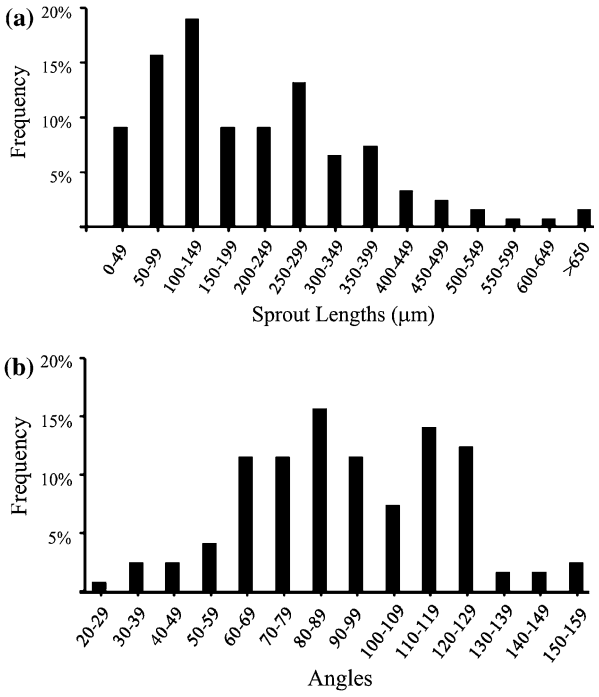

FIGURE 2. Histograms of measured sprouting vessel length and branching angles. (a) Sprout lengths from adult rat mesentery networks were skewed right from the mean of 220 ± 170.3 μm. (b) The branching angles of measured sprouts were normally distributed around the mean of angle 93 ± 27.6°.

Fixable 40 kDa FITC-dextran injection identified lumens of PECAM positive vessels along the hierarchy of microvascular networks in adult male rat mesentery, including blind-ended lumens along capillary sprouts (Fig. 1). Along 121/121 sprouts, PECAM positive endothelial cells extended past the dextran labeled blind-ended lumen (Fig. 1). As an indication of the heterogeneity in sprout lumen geometries, FITC-dextran positive lumens along capillary sprouts ranged in length from 7.7 to 1115.4 μm and sprout angle off a host vessel ranged from 28.97 to 158.55° (Fig. 2). The average sprout lumen length was 220.0 ± 170.3 μm. The average sprout lumen diameter was 5.9 ± 2.0 μm. The average host vessel diameter was 10.8 ± 4.8 μm, and the average sprout angle off host vessel was 93.0 ± 27.6° (Table 1).

Capillary Sprout Models

The fluid velocity and shear stress distribution were computed in a blind-ended channel originating from a host vessel for three types of boundary conditions: non-permeable vessel wall (model 1), uniformly permeable vessel wall (model 2), and non-permeable vessel wall with open slots (model 3). For model 1, the walls of the host and blind-ended vessels were defined to be solid, thus ensuring that the flow rates at the inlet and outlet of the host vessel were equal. For model 2, the walls of the host and blind-ended vessels were defined as thin porous layers. In this model, the effective transmural outflow was uniformly distributed along the host and blind-ended vessel walls. By conservation of mass, the flow rate at the outlet of the host vessel was smaller than the flow rate at the inlet. Model 3 is a combination of models 1 and 2 and accounts for effective transmural outflow at specific locations, such as endothelial clefts. Here, the walls of the host and blind-ended vessels were defined as non-permeable

TABLE 1. Measured sprout lumen characteristics and dimensions of the geometries used in each simulation.

	D_s (μm)	D_h (μm)	L_s (μm)	θ (°)	L_h (μm)
Mean	5.9 ± 2.0	10.8 ± 4.8	220.0 ± 170.3	93.0 ± 27.6	–
Minimum	1.5	3.7	7.7	29.0	–
Maximum	10.9	34.4	1115.4	158.6	–
Simulation	6	11	50	90	200

Sprout length, sprout diameter, host vessel diameter, and sprout angle from the host vessel were measured on images of FITC-dextran filled lumen using ImageJ software. The dimensions used for the simulations were determined from the measured sprout lumen characteristics. The mean sprout (D_s) and host vessel (D_h) diameters were rounded to 6 μm and 11 μm. 90° was chosen to represent the mean of measured angles from the host vessel. 50 μm was chosen as the sprout length used for simulations to represent a sprout early in angiogenesis. 400 μm was chosen for the long sprout case as approximately one standard deviation above the mean. The angled sprout case was approximately the minimum acute angle observed. Means are shown ± standard deviation.

except at discrete open slot regions characteristic of finite thickness porous zones.

Fluid outflow in porous regions was assumed to obey Darcy's law:

$$\Delta p = -\frac{\mu}{\alpha} v \Delta m \tag{1}$$

where Δp is the pressure drop across the wall; v and μ are the velocity and viscosity of the fluid; Δm represents the thickness of a porous zone; and α is the permeability coefficient of the porous medium, measured in m^2. Given that hydraulic conductance L_p is defined as,

$$L_p = -\frac{v}{\Delta p} \tag{2}$$

the following relationship between α and L_p can be deduced:

$$\alpha = \mu \Delta m L_p \tag{3}$$

Consequently, either L_p or α characterizes the transmural outflow through vessel walls.

L_p was set to 0.018 μm s^{-1} $mmHg^{-1}$ ($\approx 1.35 \times 10^{-10}$ m s^{-1} Pa^{-1}), which matches mean filtration coefficient measurements along capillaries in cat mesentery.[13] The thickness of the membrane, Δm, was assumed to be 0.3 μm and the viscosity, μ, of plasma in the capillary was assumed to be 0.0012 Pa s. Based on these values and Eq. (3), α equaled 4.87×10^{-20} m^2 for the runs of model 2. The permeability coefficient in open slots for model 3 was determined by matching the rate of fluid leakage through the slots with the total transmural outflow through the host and blind-ended vessel segments in model 2. Slots with a thickness of 0.5 μm were positioned 50 μm upstream and downstream of the sprout entrance and half way to the sprout blind end.

The 3D geometries were constructed using ANSYS ICEMCFD 10.0 (ANSYS, Inc., Canonsburg, PA). Both the sprout and the host vessel were modeled as straight tubes with dimensions representative of capillary sprout geometries measured from rat mesenteric microvascular networks (Table 1). Table 1 also indicates the geometric values selected for the simulations. For this study, our focus was to determine the shear stress distribution along the length of capillary sprout during the initial capillary sprouting process. We selected $L_s = 50$ μm as the sprout length since this value was representative of an initial or minimum length observed for sprouts with lumens (Fig. 2). In order to examine the influence of sprout angle θ and sprout length, additional simulations were run for the uniform permeability model with a sprout angle of 30° and a sprout length of 400 μm, respectively. In these simulations all other model parameters remained the same: host vessel length, $L_h = 200$ μm, host vessel diameter, $D_h = 11$ μm, and sprout diameter, $D_s = 6$ μm.

For all simulations, the computational domain was filled with unstructured hybrid meshes (combined with hexahedral and tetrahedral meshes) (Fig. 3). The total number of grid cells used per simulation was approximately 558,112. Four grid layers were assigned to porous zones (Fig. 3. Model 2-b, c), while eight grid layers were used for permeable slots (Fig. 3. Model 3-b). Additional grid cells were used in the slotted regions compared to the porous zones because of an increased velocity gradient due to the matched total out-flux constraint. In order to justify the number of grid cells used in our study, we conducted a mesh independence test. We compared the WSS data for the selected mesh density with the data from coarse and fine mesh simulations (grid cell numbers are 132,644 and 2,828,808, respectively). As seen in Fig. 4, there is a close agreement in the simulation data between the selected and fine mesh densities (5% error), excluding

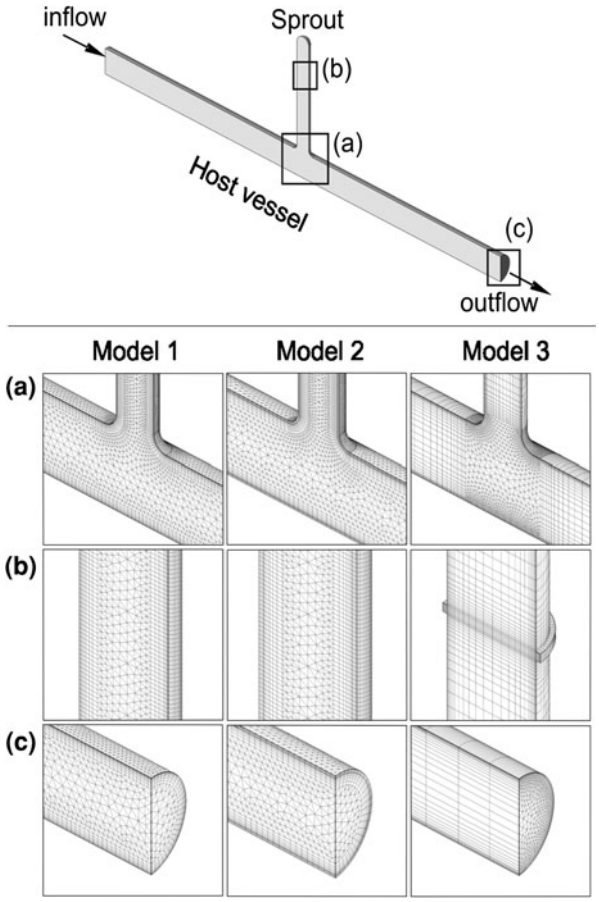

FIGURE 3. Representative geometry and local magnified mesh schemes per vessel wall model type for a 50 μm long, 6 μm diameter sprout branching at 90° from an 11 μm diameter host vessel.

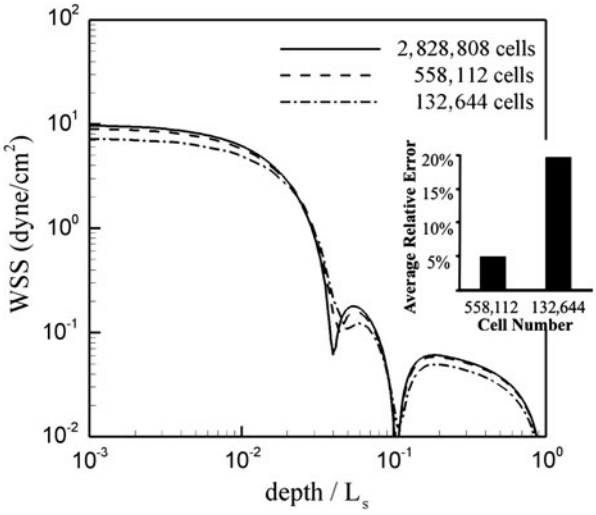

FIGURE 4. Mesh independence study of wall shear stress on a uniformly permeable blind-ended channel along the axis of the host vessel. 558,112 cells were used for the remaining simulations, and maintained an average error less than 5% from simulations run with 2,828,808 cells, except at flow separation points. Flow separation points are represented by local shear stress minimums, and occur below physiologically relevant shear stress levels.

stagnation-point flow regions shown in the WSS plot as sudden depressions. The use of the coarse mesh leads to 20% error in the WSS calculation. We considered the absolute value of the shear stress at the vessel wall, i.e., WSS is non-negative everywhere and equal to zero only at stagnation points. Sudden depressions in the WSS vs. sprout depth curves indicate the location of stagnation planes that separate two neighboring flow vortices in a sprout.

For all cases, the velocity profile imposed at the inlet boundary is Poiseuillian with an average fluid velocity U equal to 1 mm/s, which is in the range of previously observed mean velocities of blood in capillary segments.[27] At the outlet of the host vessel, we imposed a uniform static pressure of 10 mmHg. For this study, we considered the flow of either a cell free solution (blood plasma) or a solution containing a single rigid red blood cell (RBC) of biconcave shape. Blood plasma was modeled as an incompressible Newtonian fluid with density, ρ, equal to 1050 kg/m^3 and shear viscosity, μ, equal to 0.0012 Pa s (1.2 cp). The flow field is laminar because the Reynolds number for blood flow in capillaries is very low. Based on these assumptions, the following 3D steady-state Navier-Stokes equations were used as the governing equations.

$$\text{Mass:} \qquad \nabla \cdot \mathbf{V} = 0 \tag{4}$$

$$\text{Momentum:} \qquad \rho \mathbf{V} \cdot \nabla \mathbf{V} = -\nabla p + \mu \nabla^2 \mathbf{V} \tag{5}$$

All simulations were run using ANSYS Fluent 12.0 (ANSYS, Inc., Canonsburg, PA). For two permeable models, the outside surfaces of the porous layer and the slots were defined as pressure outlet boundaries with a static pressure equal to zero. The governing equations (Eqs. (4) and (5)) were solved with the above boundary conditions in Fluent with the SIMPLE method. The computation was carried on a Dell Precision T3500 workstation (Dell Inc. Round Rock, TX) with a Xeon Quad-CPU@2.6 GHz and 6 GB RAM under 64-bit Windows XP (Microsoft Corp. Redmond, WA). Double precision data type was used and the computational runs were performed with 4 parallel processes. Each simulation lasted 2–2.5 h for all the residuals to be less than 10^{-12}. The WSS was defined as the magnitude of the wall shear stress vector $\boldsymbol{\tau}_w$, which is the product of the shear stress tensor $\boldsymbol{\tau}$ and the normal vector of the wall surface $\mathbf{n}$,

The wall shear stress gradient (WSSG) was calculated as follows:

$$\text{WSS} = \|\boldsymbol{\tau}_w\| = \|\boldsymbol{\tau} \cdot \mathbf{n}\| = \sqrt{\left(\tau_{xx}n_x + \tau_{xy}n_y + \tau_{xz}n_z\right)^2 + \left(\tau_{yx}n_x + \tau_{yy}n_y + \tau_{yz}n_z\right)^2 + \left(\tau_{zx}n_x + \tau_{zy}n_y + \tau_{zz}n_z\right)^2} \tag{6}$$

$$\text{WSSG} = \|\nabla\tau\|_w = \sqrt{\left(\frac{\partial\tau}{\partial x}\right)_w^2 + \left(\frac{\partial\tau}{\partial y}\right)_w^2 + \left(\frac{\partial\tau}{\partial z}\right)_w^2} \tag{7}$$

in which

$$\tau = \|\boldsymbol{\tau}\| = \mu\sqrt{\frac{\mathbf{D}:\mathbf{D}}{2}} \text{ and } \mathbf{D} = \nabla\mathbf{v} + (\nabla\mathbf{v})^{\mathrm{T}} \tag{8}$$

In order to investigate the RBC influence on the shear stress distribution along a permeable capillary sprout, we used Fluent's Dynamic Mesh Method to incorporate a single RBC into Model 2. The cell with its center of mass located on the centerline of the host vessel was passed by the sprout entrance. The Dynamic Mesh Method consisted of two steps:

1. Determination of the RBC speed with the Six Degree of Freedom (6DOF) model [ANSYS Inc., ANSYS FLUENT 12.0. User's Guide, 2009): The RBC was located initially in the host vessel 30 μm away from the sprout in the

upstream direction, while plasma flowed around it. Then, the RBC was released and allowed to move downstream under the hydrodynamic force imposed by the plasma flow. At each time step, the force and moment applied to the RBC was calculated and then substituted into the linear and angular momentum equations to find the translational and angular accelerations of the cell. For a time step of 10^{-8} s, the RBC reached a constant translational speed within approximately 3×10^{-6} s.

2. Simulation of the RBC motion using the value of the translational speed determined in Step 1: The cell was then given a constant axial velocity and passed along the host vessel. The time step for this simulation was set to 10^{-5} s and the data was saved every 100 time steps for further analysis.

In this study, the RBC was modeled as a rigid axisymmetric body of revolution (the axis of revolution coincides with the centerline) which biconcave shape was described according to the formula proposed by Evans and Fung[12]:

$$\frac{D(r)}{C_0} = \sqrt{1 - \left(\frac{r}{R_0}\right)^2}\left[1 + \frac{C_2}{C_0}\left(\frac{r}{R_0}\right)^2 + \frac{C_4}{C_0}\left(\frac{r}{R_0}\right)^4\right] \quad (7)$$

Here r is the radial coordinate (distance from the cell center to a specific point on the plane of revolution), D is the RBC thickness that depends on the radial coordinate, $R_0 = 4$ μm is the RBC radius (maximum value of r), $C_0 = 1$ μm is the minimum thickness of the RBC (at $r = 0$), and $C_2 = 7.7$ μm and $C_4 = -5.0$ μm are nonlinear shape parameters of the RBC.

To estimate the influence of the RBC trapped in a sprout on the local shear stress distribution, we have performed an additional simulation in which the plugged RBC was located halfway along the sprout. The shape of the plugged RBC was assumed to be an ellipsoid with radii in the cross section of the sprout $r_1 = r_2 = 3$ μm. The longest radius of the ellipsoid (along the sprout) was determined from the conservation of volume:

$$r_3 = \frac{V_{\mathrm{RBC}}}{4r_1r_2/3} = \frac{3\int_0^{R_0} 2\pi r D(r)dr}{4r_{\mathrm{sprout}}^2} \quad (8)$$

From Eqs. (7) and (8) it follows that $r_3 = 2.61$ μm.

RESULTS

Capillary Sprout Models: Plasma Only Flow

Based on the identification of capillary sprout lumens and their geometric characteristics in the rat mesenteric microvascular networks, fluid velocity profiles and corresponding WSS values were computed for a 50 μm long, 6 μm diameter sprout branching off an 11 μm diameter host vessel at 90°. Figure 5 shows the results of these simulations for three vessel wall models: a non-permeable wall (Figs. 5a–5c), a uniformly permeable wall (Figs. 5d–5f), and a non-permeable wall with open slots in the sprout and host vessel (Figs. 5g–5i). Flow in the host vessel upstream and downstream of the sprout displayed a parabolic profile with the centerline velocity of 2 mm s^{-1} (Figs. 5a, 5d, and 5g). The inlet WSS in the host vessel was 8.9 dyne cm^{-2} in the non-permeable and open slot models, and 6.3 dyne cm^{-2} in the uniformly permeable wall case. The decrease in inlet WSS can be explained by the outflow through the host vessel wall (Figs. 5b, 5e, and 5h).

For the non-permeable sprout (model 1), the WSS reached a maximum of 13.9 dyne cm^{-2} at the sprout entrance and then decreased to below 0.2 dyne cm^{-2}, a shear stress threshold for endothelial cell activation,[5] within 4.1 μm into the sprout (Fig. 5c). This figure also shows that the WSS has a local minimum at a depth of 1.2 μm. As already mentioned, local minimums or inflections in the distribution of WSS values along the length of the sprout represent local changes in flow direction due to the recirculation zones. According to Fig. 5a, there are three recirculation zones (vortices) along the blind-ended non-permeable sprout. This is consistent with classic cavity flow models.[31]

In the uniform permeability case (model 2), the maximum WSS at the sprout entrance was 8.9 dyne cm^{-2} (Fig. 5f) and the depth into the sprout, at which the shear stress decreased below 0.2 dyne cm^{-2}, was essentially the same (4.2 μm) as for the non-permeable sprout (4.1 μm). Wall permeability plays an important role in the flow field inside the sprout. Specifically, it decreases the number of vortices and leads to flow asymmetry (compare Figs. 5a and 5d), which in turn results in different WSS distributions between the upstream and downstream sides of the sprout (Fig. 5f). In this simulation, the hydraulic conductivity of the vessel wall was 0.018 μm s^{-1} $mmHg^{-1}$. This value represents the filtration coefficient of cat mesenteric capillaries[13] and the upper limit for permeability coefficients of normal frog and rat mesenteric capillaries stimulated with VEGF,[3,26] which is the primary regulator of sprouting angiogenesis.[18] Additionally, our analysis of the permeability effects indicates that when the hydraulic conductivity decreases to 0.0036 μm s^{-1} $mmHg^{-1}$ (within the range of values for unstimulated capillaries), a change in the distribution of WSS above its threshold value remained negligibly small (compare short-dashed and solid lines in Fig. 6). Wall permeability effects on WSS magnitudes become

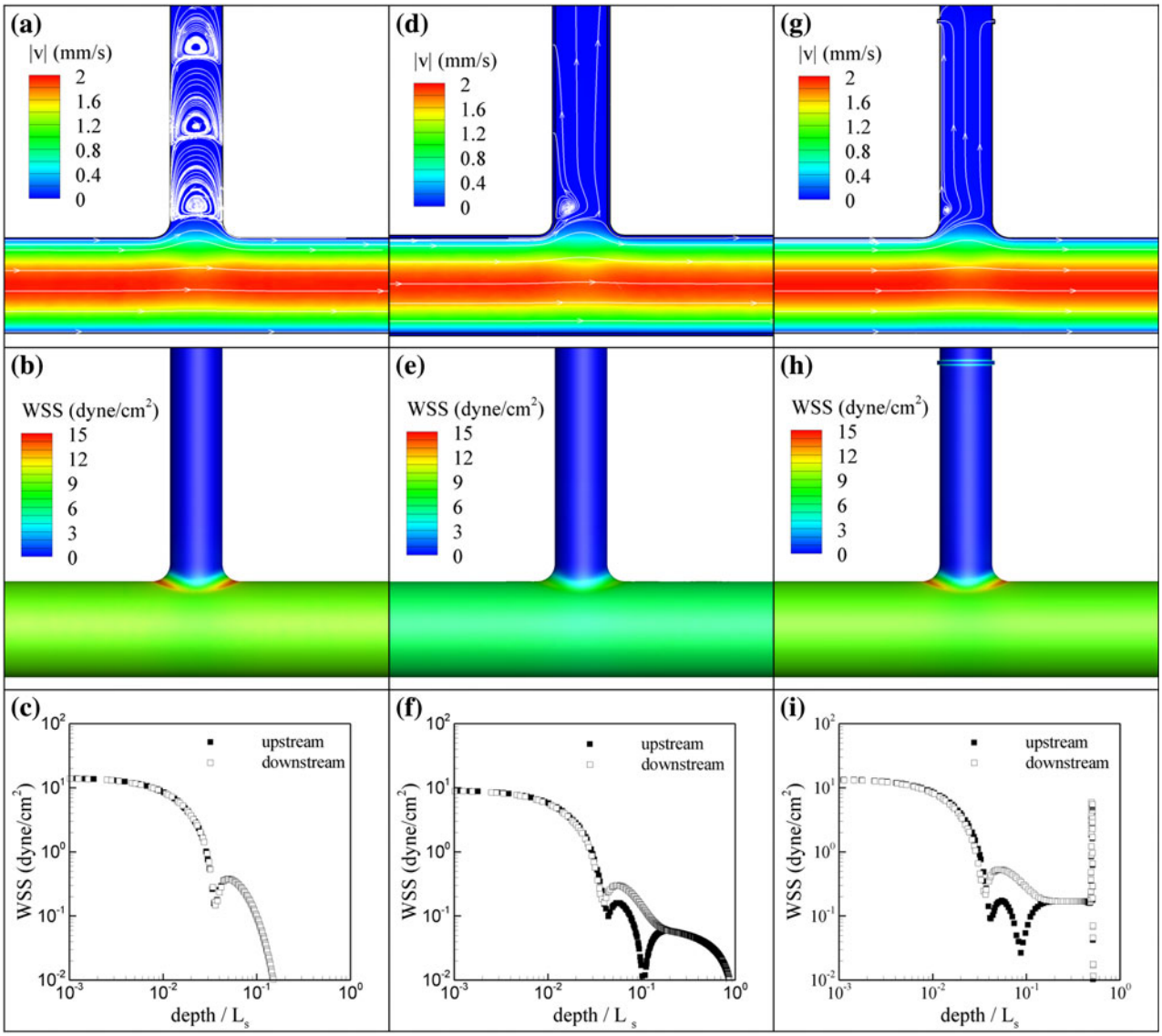

FIGURE 5. Three-dimensional analysis of fluid flow in a 50 μm long, 6 μm diameter sprout branching at a 90° angle from an 11 μm diameter host vessel for three cases of permeability: Non-permeable wall case (a–c), uniform wall permeability case (d–f) and non-permeable with simulated endothelial cleft case (g–i). Velocity profiles and streamlines are plotted in two dimensions in the system's coronal plane (a, d, g). Multiple vortices form along the length of the blind-ended channel in the non-permeable wall case (a), while for the permeable cases, single vortices form on the upstream blind-ended channel entrance (d, g). Wall shear stress magnitudes are plotted on three dimensional color maps (b, e, h). For each permeability simulation, shear stress maximums occur at the entrance of the blind-ended channel, compared to the upstream and downstream host vessel wall shear stress. Wall shear stress magnitudes are plotted over the blind-ended channel length on the line intersected by the coronal plane (c, f, i). Shear stresses within the sprout channel are negligible for the non-permeable and uniformly permeable wall cases, but spikes near simulated endothelial cell clefts (i).

apparent when hydraulic conductivity increases by an order of magnitude from its baseline (long-dashed and dash-dot-dot lines).

As in the case of the uniformly permeable wall model (model 2), the velocity field inside the non-permeable sprout with open slots (model 3) is characterized by one asymmetric vortex near the upstream side of the sprout (Fig. 5g), which again leads to the asymmetry in the shear stress distribution between the upstream and downstream walls of the sprout (Fig. 5h). The open slots model predicts similar values of the maximum WSS and the threshold depth as the non-permeable model. However, the WSS reached a local maximum of 5.9 dyne cm^{-2} at the slots. This indicates the potential for endothelial cells near the clefts to be activated by shear stresses, even if these cells are located deep into the sprout.

To identify the potential importance of sprout geometries on the WSS distribution, we also simulated flow in a uniformly permeable capillary sprout 1)

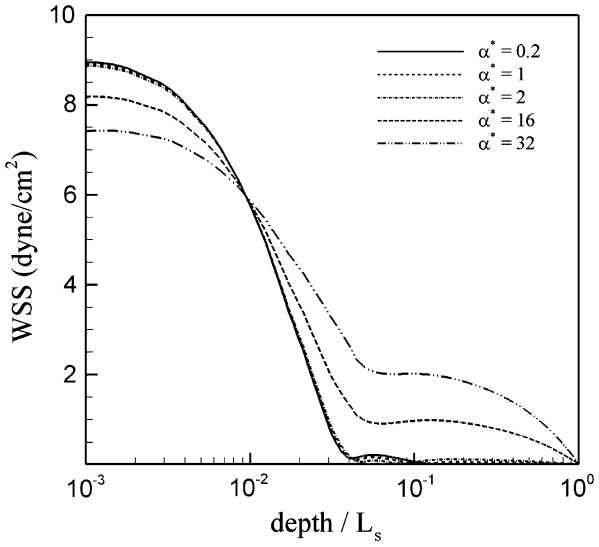

FIGURE 6. Wall shear stress distribution along the sprout length for a range of permeability constants. Shear stresses within the blind-ended channel increase in magnitude as channel wall permeability increases, but decrease at the sprout entrance. The permeability range within rat mesenteric microvascular networks is on the scale of $\alpha^* = .2$ to $\alpha^* = 1$. Shear stress magnitudes across the system do no significantly change unless the permeability is increased by an order of magnitude ($\alpha^* = 16$, $\alpha^* = 32$). Here $\alpha^* = \alpha/\alpha_{baseline}$, where $\alpha_{baseline} = 0.018\ \mu m\ s^{-1}\ mmHg^{-1}$.

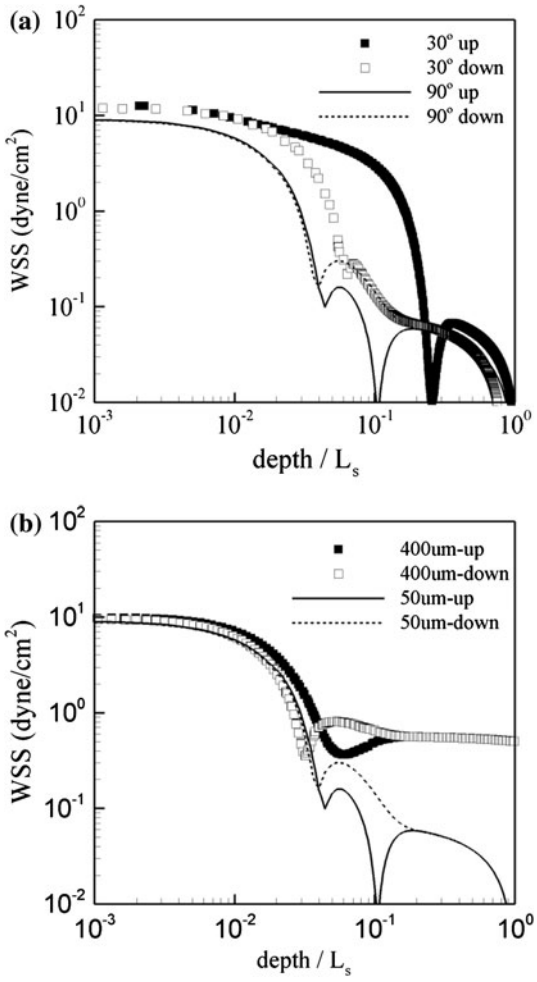

FIGURE 7. Wall shear stress distribution along the sprout length for a (a) sprout branching at 30° from the downstream host vessel wall and (b) a 400 μm long sprout. The branching angle alters the shear stress distribution by increasing the length into the sprout where relevant shear stresses occur to slightly over 10% of the sprout length on the upstream wall. The increase in sprout length increases the wall surface area and flow through the sprout wall, resulting in increased flow into the sprout and an increase in shear stress magnitudes along the entire length of the sprout to physiologically relevant levels.

branching off the host vessel at 30° and 2) with a 400 μm length (Fig. 7). A change of the sprout angle from 90° to 30° led to an increase in the maximum WSS from 8.9 to 12.9 dyne cm^{-2} (Fig. 7a). While flow asymmetry along the upstream vs. downstream sides of the sprout did not influence the threshold depth for the 90° sprout (Fig. 5f), it did lead to different threshold depths for the upstream and downstream sides of the 30° sprout (10.5 μm for the upstream wall and 4.2 μm for the downstream wall). An increase in the length of the permeable sprout from 50 to 400 μm led to an increase in the WSS above the threshold value of 0.2 dyne cm^{-2} for the whole length of the sprout (open and closed squares in Fig. 7b). This result can be explained by the increased fluid flux through a longer sprout due to a larger surface area available for fluid filtration. This case highlights the potential for endothelial cells to experience relevant shear stress magnitudes during later stages of capillary sprouting.

Capillary Sprout Models: Effect of a Red Blood Cell

Figures 8 and 9 depict the flow field and WSS distribution in the host vessel and capillary sprout in the presence of a single, rigid RBC, according to the uniform wall permeability model (model 2). In Fig. 8, the RBC was positioned in the center of the host vessel and its passage by the entrance of the capillary sprout was simulated by the Dynamic Mesh method (see "Materials and Methods" section). As evident from the velocity data, the passing RBC distorts the recirculation zone in the sprout. The flow vortex originally located near the upstream wall of the sprout (Fig. 8a) was moved to the sprout center when the RBC passed by the axis of the sprout (Fig. 8d). As soon as the RBC moved out of the sprout region, the vortex position was restored (Fig. 8g). This distortion, however, had a small effect on the WSS (Figs. 8b, 8e, and 8h). There is an increase in the maximum WSS from 8.9 to 9.6 dyne cm^{-2} and in the threshold depth from 4.2 to 4.5 μm (Figs. 8c, 8f, 8i).

The RBC trapped inside the sprout (Fig. 9a) effectively decreases the sprout volume. This led to small

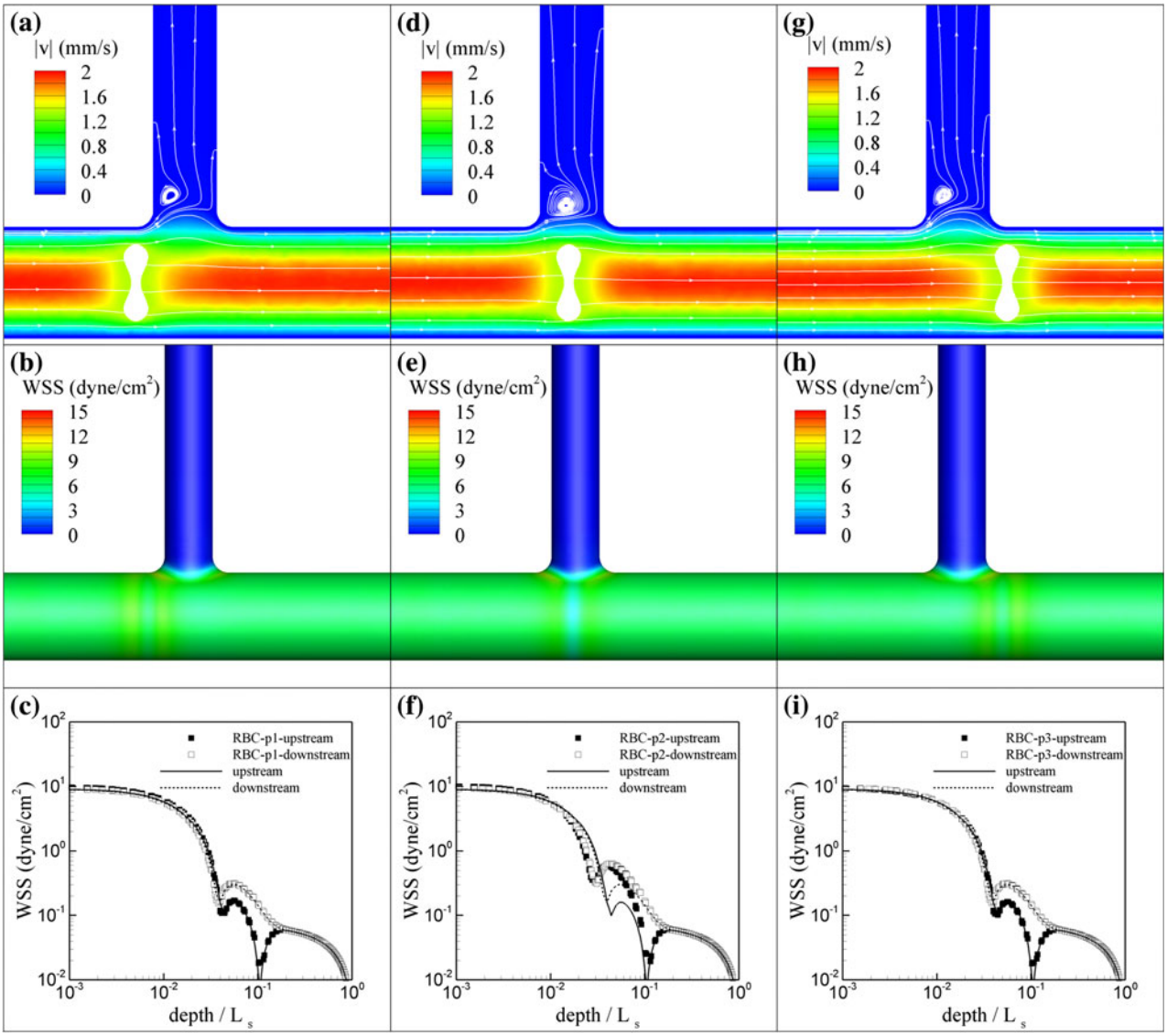

FIGURE 8. Three-dimensional analysis of fluid flow in a 50 μm long, 6 μm diameter uniformly permeable sprout branching at a 90° angle from an 11 μm diameter host vessel with a red blood cell fixed at position 1 (p1) upstream from the sprout entrance (a), position 2 (p2) at the sprout entrance (d), and position 3 (p3) downstream from the sprout entrance (g). As the red blood cells flows through the host vessel, local maximums occur in front, and behind the red blood cell, as described by Xiong and Zhang (b, e, h).[39] The shear stress distribution within the blind-ended channel does not change for p1 (c) and p3 (i). However, as the red blood cell passes by the sprout entrance, shear stresses slightly increase according to the peak-valley-peak trend observed as the cell flows through the host vessel. Additionally, the vortex at the entrance shifts slightly towards the center of the sprout, shifting the flow separation points (f). Despite the shift in shear stress distribution due to a passing red blood cell, the actual effect of an individual cell may be negligible in time scale, and shear stress magnitude.

changes in the maximum WSS (from 8.9 to 9.8 dyne/cm^2) and threshold depth (from 4.2 to 4.0 μm) (Fig. 9b). At the corner regions between the plugged RBC and the sprout wall WSS magnitudes jump above the threshold value (Fig. 9b). In these regions with decreasing spacing between the RBC surface and the wall, flow accelerates because of volume conservation. This result indicates that plugged RBCs can be a source of endothelial cell activation during capillary sprouting through their generation of local WSS maximums.

Finally, Fig. 10 compares the WSSG data between the cases of plasma only flow and plasma flow with a passing RBC for the uniformly permeable vessel wall conditions. For plasma only flow, the gradient of the wall shear stress reached a maximum of 50 dyne cm^{-2} μm^{-1} at the sprout entrance and then rapidly drops to zero further into the sprout (Fig. 10a). As the RBC passed by the sprout entrance, the region of high WSSG extended immediately upstream and downstream along the host vessel (Fig. 10b).

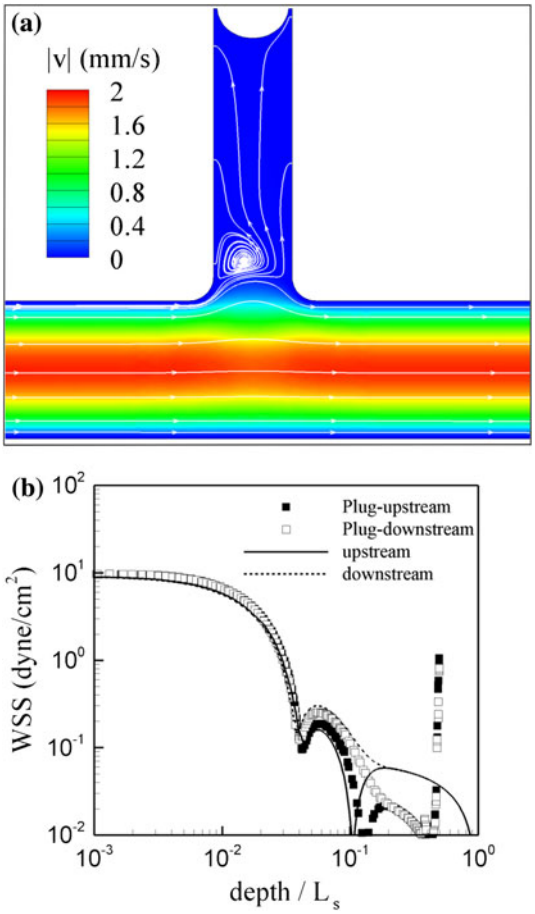

FIGURE 9. Three-dimensional analysis of fluid flow in the standard geometric configuration with uniform wall permeability and a red blood cell fixed within the sprout. The velocity profile and streamlines are plotted in two dimensions in the system's coronal plane (a). The velocity profile is similar to the uniform wall permeability case. Wall shear stress magnitudes are plotted over the channel length on the line intersected by the coronal plane (b). Near the plugged red blood cell, shear stresses begin to increase to physiologically relevant magnitudes.

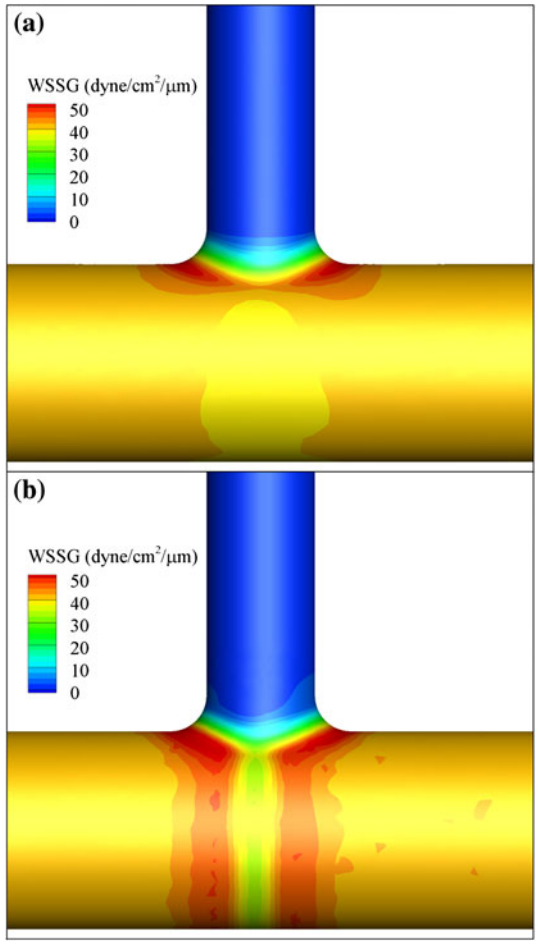

FIGURE 10. Three-dimensional gradient analysis. (a) Wall shear stress gradients are plotted for the uniform wall permeability case without a red blood cell, and (b) with a red blood cell in the host vessel at the axis of the sprout. As expected, high shear stress gradients occur at the sprout entrance for both cases. In the case including a red blood cell, the gradient occurs in a peak-valley-peak profile across the length of the red blood cell.

DISCUSSION

The primary contribution of this study is the estimation of fluid shear stress magnitudes along the length of a permeable capillary sprout for various physiological scenarios. Previous computational fluid dynamics models have evaluated RBC deformation and the influence of local pressure and velocity profiles within capillary tubes, but have not focused on flow conditions within a capillary sprout.[2,30,34,37–39] The recent identification of fluid flow in blind-ended vessels suggests a functional role of fluid shear stresses within them[19], yet in part due to the technical difficulty associated with observing velocity fields within capillary sprouts *in vivo*, the determination of local shear stresses has remained uncertain. Our findings identify local WSS magnitude and gradient maximums at the sprout entrance and suggest that during initial sprouting endothelial cells within the sprout do not experience WSS. Interestingly, plasma only flow through longer sprouts and sprouts with transmural flux at endothelial cell clefts did result in potential physiologically relevant WSS magnitudes. RBC plugging also accounted for WSS stimuli within sprouts. Thus, over the time course of capillary sprouting, endothelial cells can experience WSS stimuli depending on their position along the sprout, sprout length, how fluid flows across the capillary wall, and whether the sprout is plugged by a RBC. The spatial distribution of WSS along sprouts for these different scenarios provides relative input magnitudes that can be used in investigations aimed at mechanistically identifying how WSS influences endothelial cell function during angiogenesis and highlight the need to better

understand the integrated cellular and fluid dynamics associated with sprout lumen formation.

Our work offers a three-dimensional estimation of relative shear stress magnitudes based on physiologically relevant capillary sprout geometries from adult rat mesenteric microvascular networks undergoing normal angiogenesis associated with tissue growth. While a dynamic time-lapse study is required to confirm that the blind-ended vessels analyzed in this study are in fact sprouting, previous characterizations of angiogenesis in rat mesenteric tissue suggest that these structures are indicative of a vessel growth process.[1,25] In our model, the average inlet velocity in the host vessel was assumed to be constant at 1 mm/s, which is in the range of previously observed mean velocity in capillary segments.[27] An increase in fluid velocity in the host vessel would lead to higher WSS at the sprout entrance, but would cause insignificant changes in the WSS within the sprout assuming the hydraulic conductivity of the sprout wall remained the same and the sprout length did not change.

According to *in vitro* flow chamber experiments,[5] endothelial cells respond to WSS magnitudes as low as 0.2 dyne cm^{-2}. While we consider this value as the threshold for endothelial cell activation by fluid flow, specific thresholds would need to be identified per cellular response of interest. In our simulation of plasma flow in a non-permeable capillary sprout, the WSS drops from its maximum value at the sprout entrance to the threshold value within about 4 μm into the sprout. This threshold depth remained essentially the same for a uniformly permeable sprout when the hydraulic conductivity is in the range for unstimulated and VEGF-stimulated capillaries. Generally, an increase in the permeability of the sprout wall leads to a higher flow rate into the sprout and thus a larger threshold depth, but this effect becomes pronounced when the hydraulic conductivity is at least one order of magnitude higher than the baseline for stimulated vessels or when the sprout is sufficiently long.

The distribution of shear stresses predicted in our uniform wall permeability model indicates that endothelial stalk cells reside in low shear stress regions, and that shear stress peaks at the sprout entrance. Low, or static shear conditions (0–5 dyne/cm^2) are associated with endothelial cell proliferation, and DNA synthesis.[11,22] The results of our simulation suggest that stalk cells are in shear stress zones that permit proliferation, which is consistent with the current understanding of sprouting dynamics.[17] Local maximum shear stress magnitudes which occur at the sprout inlet may be linked to cellular dynamics associated with initial cell migration and paracrine signaling. For example, step changes in shear stress have been shown to induce remodeling of focal adhesions and cytoskeletal structure *in vitro*.[9] Interestingly, observations by us (data not shown) and previously by Rhodin and Fujita in rat mesenteric microvascular networks indicate that vascular pericytes, which are recruited and support endothelial cells, are frequently located at capillary-sprout bifurcations.[28] The local recruitment of pericytes at these locations of increased shear stress is supported mechanistically by evidence that the shear stress stimulation of endothelial cells causes platelet-derived growth factor production, along with other soluble factors, in endothelial cells.[5,9,24]

Shear stress gradients have been implicated in the triggering of atherosclerosis by influencing endothelial cell dynamics[20] associated with angiogenesis. Evidence that shear stress gradients directly influence angiogenic endothelial cell dynamics is supported by *in vitro* disturbed flow experiments. From our plasma flow simulation with uniform permeability conditions, we predict a maximum shear stress gradient of 50 dyne cm^{-2} μm^{-1} at the sprout entrance. In response to shear stress gradients lower than those predicted by the model, endothelial cells migrate away from shear gradients, and increase motility and proliferation.[8,10,36] The shear stress gradients at the entrance of a capillary sprout undoubtedly depends on the inlet geometry and radius of curvature for the branching blind-ended side channel. The exact physiological measurement for this parameter in our model remains unknown. We speculate that a decreased radius would result in increased local maximum shear stress values and a steeper inlet gradient. Nonetheless, given the probable range of physiologically relevant inlet geometries, our results identify the presence of a local gradient capable of initiating an endothelial response.

Another important result of our study is the prediction of high shear stresses at open slots (i.e., inter-endothelial clefts), indicating that these openings in the sprout wall may serve as locations where endothelial cells within the sprout may be activated by fluid flow. Interestingly, Tarbell *et al.* predicted shear stress magnitudes up to 50 dyne/cm^2 between capillary endothelial cells in a model of flow through inter-endothelial cell clefts.[35] The simulation data obtained with the open slots and uniform permeability models both highlight the potential influence of shear stresses localized to endothelial cell junctions on whole cell behavior during angiogenesis, especially in a tumor microenvironment, in which capillaries are characterized by hyper-permeability and have large inter-endothelial junctions.[14]

We recognize that the plasma only flow simulation represents a simplified case and does not account for the presence of RBCs. The relevance of the plasma only simulation is supported by the identification of ''silent capillaries,'' defined as having only plasma flow

due to plasma skimming, during observation of blood flow through microfabricated microvascular networks.[32] A transient presence of plasma only flow is also supported by the heterogeneity of RBC flux through single capillaries within a microvascular network and the observation of single RBCs intermittently flowing through capillaries.[15,29,40] In our study, the identification of vessel lumens via dextran injection and fixation allows for identification of RBC presence due to the cell shaped voids of dextran labeling in smaller caliber vessels. Previous analysis using this method along with the analysis of our specimens (data not shown) identifies examples of capillaries sprouts void of RBCs.[19] More importantly, even in considering plasma only flow, we identified local WSS maximums at the sprout entrance and scenarios (increased sprout length and permeability at inter-endothelial clefts) that result in potential WSS stimuli for endothelial cells within a sprout.

In order to evaluate the associated non-continuum, non-Newtonian flow effects due to RBC-plasma interactions, we also simulated a rigid RBC passing by the entrance of a capillary sprout and a plugged RBC within a sprout. Results from this dynamic simulation identify local WSS peaks upstream and downstream of the RBC. This agrees with the study by Xiong and Zhang in which the shear stress distribution along the capillary wall was estimated from the simulation of deformable RBCs flowing in narrow capillaries.[39] Additionally, our data show that the passage of a RBC past the sprout entrance increases the shear stress at the sprout entrance by 7.8% (8.9–9.6 dyne/cm^2) and shifts the threshold depth further into the sprout by 7.1% (4.2–4.5 μm). Future experimental studies are necessary to determine whether these effects on WSS distribution influence endothelial cell dynamics. Our simulation of a plugged RBC within a sprout identifies a scenario that endothelial cells adjacent to the curved plugged cell experience a local spike in shear stress. These results emphasize the importance of future work focused on investigating RBC deformation and RBC flow dynamics during capillary sprout growth.

In summary, our work provides an estimation of relative shear stress magnitudes along the lumen of a capillary sprout. During the early stages of capillary sprouting, the endothelial cells at the sprout entrance experience increased shear stress relative to upstream and downstream values. Within the capillary sprout cells experience negligible shear stresses along the majority of the sprout. However, shear stresses become relevant for longer sprouts during later stages of sprout growth and when transmural outflux occurs at local endothelial cell junctions. Our results provides valuable insight into shear stress stimuli involved in capillary sprouting and serve to motivate experimental work focused on linking this mechanical cue to endothelial cell dynamics associated with angiogenesis.

ACKNOWLEDGMENTS

This work was supported by Louisiana Board of Regents grants LEQSF(2007-12)-ENH-PKSFI-PRS-01 (D. Khismatullin) and LEQSF(2009-12)-RD-A-19 (W. Murfee).

REFERENCES

[1]Anderson, C. R., A. M. Ponce, and R. J. Price. Immunohistochemical identification of an extracellular matrix scaffold that microguides capillary sprouting in vivo. *J. Histochem. Cytochem.* 52:1063–1072, 2004.

[2]Barber, J. O., J. P. Alberding, J. M. Restrepo, and T. W. Secomb. Simulated two-dimensional red blood cell motion, deformation, and partitioning in microvessel bifurcations. *Ann. Biomed. Eng.* 36:1690–1698, 2008.

[3]Bates, D. O. The chronic effect of vascular endothelial growth factor on individually perfused frog mesenteric microvessels. *J. Physiol.* 513(Pt 1):225–233, 1998.

[4]Chen, B. P., Y. S. Li, Y. Zhao, K. D. Chen, S. Li, J. Lao, S. Yuan, J. Y. Shyy, and S. Chien. DNA microarray analysis of gene expression in endothelial cells in response to 24-h shear stress. *Physiol. Genomics* 7:55–63, 2001.

[5]Cooke, J. P., E. Rossitch, Jr., N. A. Andon, J. Loscalzo, and V. J. Dzau. Flow activates an endothelial potassium channel to release an endogenous nitrovasodilator. *J. Clin. Invest.* 88:1663–1671, 1991.

[6]Dai, G., M. R. Kaazempur-Mofrad, S. Natarajan, Y. Zhang, S. Vaughn, B. R. Blackman, R. D. Kamm, G. Garcia-Cardena, and M. A. Gimbrone, Jr. Distinct endothelial phenotypes evoked by arterial waveforms derived from atherosclerosis-susceptible and -resistant regions of human vasculature. *Proc. Natl Acad. Sci. USA* 101:14871–14876, 2004.

[7]Davies, P. F. Flow-mediated endothelial mechanotransduction. *Physiol. Rev.* 75:519–560, 1995.

[8]Davies, P. F., A. Remuzzi, E. J. Gordon, C. F. Dewey, Jr., and M. A. Gimbrone, Jr. Turbulent fluid shear stress induces vascular endothelial cell turnover in vitro. *Proc. Natl Acad. Sci. USA* 83:2114–2117, 1986.

[9]Davies, P. F., A. Robotewskyj, and M. L. Griem. Quantitative studies of endothelial cell adhesion. Directional remodeling of focal adhesion sites in response to flow forces. *J. Clin. Invest.* 93:2031–2038, 1994.

[10]DePaola, N., M. A. Gimbrone, Jr., P. F. Davies, and C. F. Dewey, Jr. Vascular endothelium responds to fluid shear stress gradients. *Arterioscler. Thromb.* 12:1254–1257, 1992.

[11]Dewey, Jr., C. F., S. R. Bussolari, M. A. Gimbrone, Jr., and P. F. Davies. The dynamic response of vascular endothelial cells to fluid shear stress. *J. Biomech. Eng.* 103:177–185, 1981.

[12]Evans, E., and Y. C. Fung. Improved measurements of the erythrocyte geometry. *Microvasc. Res.* 4:335–347, 1972.

[13]Fraser, P. A., L. H. Smaje, and A. Verrinder. Microvascular pressures and filtration coefficients in the cat mesentery. *J. Physiol.* 283:439–456, 1978.

[14]Fukumura, D., D. G. Duda, L. L. Munn, and R. K. Jain. Tumor microvasculature and microenvironment: novel insights through intravital imaging in pre-clinical models. *Microcirculation* 17:206–225, 2010.
[15]Fung, Y. C. Mechanics of erythrocytes, leukocytes, and other cells. In: Biomechanics Mechanical Properties of Living Tissues Anonymous New York. New York: Springer Science + Business Media, LLC, 1993, pp. 109–164.
[16]Galbraith, C. G., R. Skalak, and S. Chien. Shear stress induces spatial reorganization of the endothelial cell cytoskeleton. *Cell Motil. Cytoskeleton* 40:317–330, 1998.
[17]Gerhardt, H. VEGF and endothelial guidance in angiogenic sprouting. *Organogenesis* 4:241–246, 2008.
[18]Gerhardt, H., M. Golding, M. Fruttiger, C. Ruhrberg, A. Lundkvist, A. Abramsson, M. Jeltsch, C. Mitchell, K. Alitalo, D. Shima, and C. Betsholtz. VEGF guides angiogenic sprouting utilizing endothelial tip cell filopodia. *J. Cell Biol.* 161:1163–1177, 2003.
[19]Guerreiro-Lucas, L. A., S. R. Pop, M. J. Machado, Y. L. Ma, S. L. Waters, G. Richardson, K. Saetzler, O. E. Jensen, and C. A. Mitchell. Experimental and theoretical modelling of blind-ended vessels within a developing angiogenic plexus. *Microvasc. Res.* 76:161–168, 2008.
[20]Hahn, C., and M. A. Schwartz. Mechanotransduction in vascular physiology and atherogenesis. *Nat. Rev. Mol. Cell Biol.* 10:53–62, 2009.
[21]le Noble, F., D. Moyon, L. Pardanaud, L. Yuan, V. Djonov, R. Matthijsen, C. Breant, V. Fleury, and A. Eichmann. Flow regulates arterial-venous differentiation in the chick embryo yolk sac. *Development* 131:361–375, 2004.
[22]Lin, K., P. P. Hsu, B. P. Chen, S. Yuan, S. Usami, J. Y. Shyy, Y. S. Li, and S. Chien. Molecular mechanism of endothelial growth arrest by laminar shear stress. *Proc. Natl Acad. Sci. USA* 97:9385–9389, 2000.
[23]Milkiewicz, M., M. D. Brown, S. Egginton, and O. Hudlicka. Association between shear stress, angiogenesis, and VEGF in skeletal muscles in vivo. *Microcirculation* 8:229–241, 2001.
[24]Mitsumata, M., R. S. Fishel, R. M. Nerem, R. W. Alexander, and B. C. Berk. Fluid shear stress stimulates platelet-derived growth factor expression in endothelial cells. *Am. J. Physiol.* 265:H3–H8, 1993.
[25]Murfee, W. L., M. R. Rehorn, S. M. Peirce, and T. C. Skalak. Perivascular cells along venules upregulate NG2 expression during microvascular remodeling. *Microcirculation* 13:261–273, 2006.
[26]Neal, C. R., and C. C. Michel. Differing effects of Vascular Endothelial Growth Factor (VEGF) on the ultrastructure of mesenteric microvessels of frog and rat. *J. Physiol.* 506:24P, 1998.
[27]Pries, A. R., T. W. Secomb, and P. Gaehtgens. Relationship between structural and hemodynamic heterogeneity in microvascular networks. *Am. J. Physiol.* 270:H545–H553, 1996.
[28]Rhodin, J. A., and H. Fujita. Capillary growth in the mesentery of normal young rats. Intravital video and electron microscope analyses. *J. Submicrosc. Cytol. Pathol.* 21:1–34, 1989.
[29]Schmid-Schonbein, G. W., R. Skalak, S. Usami, and S. Chien. Cell distribution in capillary networks. *Microvasc. Res.* 19:18–44, 1980.
[30]Secomb, T. W., R. Skalak, N. Ozkaya, and J. F. Gross. Flow of axisymmetric red blood cells in narrow capillaries. *J. Fluid Mech.* 163:405–423, 1986.
[31]Shankar, P. N., and M. D. Deshpande. Fluid mechanics in the driven cavity. *Annu. Rev. Fluid Mech.* 32:93–136, 2000.
[32]Shevkoplyas, S. S., T. Yoshida, S. C. Gifford, and M. W. Bitensky. Direct measurement of the impact of impaired erythrocyte deformability on microvascular network perfusion in a microfluidic device. *Lab. Chip.* 6:914–920, 2006.
[33]Skalak, T. C., and R. J. Price. The role of mechanical stresses in microvascular remodeling. *Microcirculation* 3:143–165, 1996.
[34]Sugihara-Seki, M., and R. Skalak. Numerical study of asymmetric flows of red blood cells in capillaries. *Microvasc. Res.* 36:64–74, 1988.
[35]Tarbell, J. M., L. Demaio, and M. M. Zaw. Effect of pressure on hydraulic conductivity of endothelial monolayers: role of endothelial cleft shear stress. *J. Appl. Physiol.* 87:261–268, 1999.
[36]Tardy, Y., N. Resnick, T. Nagel, M. A. Gimbrone, Jr., and C. F. Dewey, Jr. Shear stress gradients remodel endothelial monolayers in vitro via a cell proliferation-migration-loss cycle. *Arterioscler. Thromb. Vasc. Biol.* 17:3102–3106, 1997.
[37]Tözeren, H., and R. Skalak. The steady flow of closely fitting incompressible elastic spheres in a tube. *J. Fluid Mech.* 87:1–16, 1978.
[38]Wang, H., and R. Skalak. Viscous flow in a cylindrical tube containing a line of spherical particles. *J. Fluid Mech.* 38:75–96, 1969.
[39]Xiong, W., and J. Zhang. Shear stress variation induced by red blood cell motion in microvessel. *Ann. Biomed. Eng.* 38:2649–2659, 2010.
[40]Fung, Y. C. Microcirculation. In: Biomechanics: Circulation Anonymous New York. New York: Springer Science + Business Media, LLC, 1997, pp. 266–332.